Computational Condensed Matter 2 (2015) 1–10

Contents lists available at ScienceDirect

Computational Condensed Matter

journal homepage: http://ees.elsevier.com/cocom/default.asp

Regular article

# First principles study of van der Waals heterobilayers

Aniekan Magnus Ukpong*

*Department of Physics, University of Pretoria, 1 Park Street, Hatfield, 0002 Pretoria, South Africa*

ARTICLE INFO

*Article history:*
Received 14 July 2014
Received in revised form
23 October 2014
Accepted 26 November 2014
Available online 27 November 2014

*Keywords:*
Heterobilayers
Graphene
Boronitrene
Electronic structure
DFT
Quasiparticle-corrections

ABSTRACT

This paper presents a comparative first principles study of van der Waals heterobilayers derived from the coupling of graphene to silicon carbide and hexagonal boron nitride monolayer. Using the local, semi-local, and van der Waals interaction-corrected density functional theory, it found that the adhesion energy of graphene on SiC and *h*-BN monolayer is invariant under dispersion corrections. On the other hand, considerably more accurate interlayer distances are obtained using the semi-empirical DFT-D3 correction, whereas non-local corrections consistently yield higher adhesion energies of 3.70 and 2.84 mRyd per carbon for graphene on SiC and *h*-BN monolayer substrates. It is also observed that the anisotropy induced band gap depends on the evolution of the stacking sequence of heterobilayers under persistent strain. It is suggested that the delicate minimisation of the overlap interactions between interlayer π-bonds induces localised charge puddles in the interfacial electronic structure and opens up a band gap. Using the dependence of the induced band gap on network anisotropy, it is shown that the size of the band gap is tunable by controlling the stacking sequence and the strength of the dipole-induced electric field within the heterobilayer interface.



## 1. Introduction

The isolation and characterization of graphene [1] has stimulated developments of the graphene transistor [2]. However, the key challenges of this technology include opening a sizeable and well-defined band gap, thus making large-area graphene transistors that can operate in the current-saturation regime and fabricating graphene nanoribbons with well-defined widths and clean edges. On the other hand, such free-standing atomic planes can be re-assembled layer by layer into designer heterostructures in a precisely chosen stacking sequence to reveal unusual properties and interesting new phenomena [3]. The interaction between graphene and its substrate introduces a broad range of structure sensitive disorder effects. For instance, the electronic structure of the van der Waals heterostructure from coupled *h*-BN/graphene/*h*-BN layers [4–6] is sensitive to the stacking order and thickness of the BN layers. Also, interlayer interactions in hybrid silicene/graphene nanocomposite layers induce charge carriers whose concentration is tunable by controlling the interlayer distance [7]. Interfacial phenomena such as formation of interface dipole [8], structural corrugation [9–12], charge puddles [13–16], and edge-localised dangling bond states [17,18] play important roles in typical transistor device applications. The absence of the band gap in graphene means that electrons always interact strongly with the substrate making charge tunable device properties hard to achieve. However, several ways of opening the band gap in graphene include the introduction of vacancies, adsorption of impurity atoms; fluorides [19] or hydrogen [20], and application of *in-plane* biaxial [21], or shear [22], strain. Other techniques include constraining the sheet in 1D to form graphene nanoribbons (GNRs). Band gaps of such GNRs vary inversely with the width of the ribbon [23]. This scheme, though viable in graphene microelectronics [24–26], is hard to integrate into current technologies for film growth. An attractive route, which can be integrated into the chemical vapour deposition (CVD) mechanism, is to engineer the growth orientation of graphene on the underlying substrate.

Graphene grows epitaxially on metallic substrates [27–32] via CVD processes but chemically-inert substrates are now attracting considerable interest due to promising new functionalities. One such substrate is boronitrene - a single layer of hexagonal boron nitride (*h*-BN) [33]. The *h*-BN monolayer has emerged as the preferred support for graphene in quantum-well heterojunctions because both are isostructural and have low lattice mismatch [34–36]. In addition, graphene has its highest electron mobility

* Present address: Johnson Matthey Technology Centre, Room 161, Floor 1, Building 22, Council for Scientific and Industrial Research (CSIR), Meiring Naude Road, Brummeria, Silverton 0127, Pretoria, South Africa.
*E-mail address:* aniekan.ukpong@matthey.com.

http://dx.doi.org/10.1016/j.cocom.2014.11.004

when placed on *h*-BN substrates compared to any other substrate [34] because of its ability to suppress charge inhomogeneities and structural disorder at the heterobilayer [10]. Moreover, its wide band gap and low chemical activity also make it a good tunnelling barrier in quantum-well heterojunctions [37]. Ultrathin *h*-BN layers are now obtainable from traditional CVD processes [38] as the preferred dielectric for graphene heterojunction transistor integration because of increased availability of high-purity single crystals *h*-BN [39]. Besides, recent measurements suggest that the existence of graphene-like silicon [40], hence the possible occurrence of monolayer SiC in atomically-thin non-polar form cannot be overruled since the monolayer structure is common to both silicon and carbon.

Graphene can also grow epitaxially on either the Si-terminated [41–43] or C-terminated [44–46] polar face of silicon carbide substrate. Thus, the SiC monolayer can support graphene quantum-well heterostructures by maintaining the atomically-flat honeycomb structure. Nevertheless, the nature of the electronic coupling between the graphene overlayer to such monolayer substrates is still not well-understood, although the electronic structure of isolated monolayers of graphite [1], SiC [47,48], and *h*-BN [49] have been widely studied. Recent investigations of the graphene/monolayer *h*-BN bilayer coupling using lattice-match and lattice-mismatch approximations indicate that the zero-band-gap feature does not depend on the translation and rotation of graphene with respect to the substrate [50]. By contrast, recent spectroscopic measurements [51,52] suggest that the electronic structure of the interfaces has significant influence on the charge transport between the two coupled monolayers.

Here, spectroscopic properties of the graphene overlayer on heterogeneous monolayers are investigated using first principles calculations based on van der Waals interaction-corrected density functional theory. The interface inhomogeneities which form under the influence of dispersive long-range interactions [53] are investigated to unravel the effects of different stacking orientations on the weak coupling of graphene with heterogeneous monolayer substrates. It is shown that a spontaneous band gap develops, under zero external field, when the number of carbon atoms with perpendicularly-aligned $\pi$-bonds is minimised. It is found that the band gap only opens when the orientation of the graphene overlayer breaks the symmetry of the $\pi$-bands with respect to the substrate, irrespective of the chemical species of the substrate. The combined effect of the interfacial electric field and van Hove singularities causes the formation of the band gap. These interfacial electronic features are identified as unique signatures of the minimization of the overlap interaction between *p*-orbitals when graphene is physisorbed on heterogeneous monolayers.

## 2. Computational method

Graphene heterobilayers have been modelled as simulated physisorption of the graphene sheet on *h*-BN (or SiC) monolayer at persistent mismatch strain. The electronic structure was calculated using the plane wave self-consistent field (PWSCF) code as implemented in quantum ESPRESSO [54]. The exchange-correlation (XC) potentials was first described in the local (LDA) and semilocal (GGA) approximations. In each case, the parameterizations of Perdew and Zunger (PZ) [55], and Perdew, Burke, and Ernzerhof (PBE) [56] were used. These two approximations for the exchange-correlation potential fail to adequately describe the long-range van der Waals interactions that exist in the layered materials considered in this study. Hence, the four variants of the van der Waals interaction-corrected density functionals were used to investigate the interlayer coupling. Firstly, the Roman-Perez and Soler implementation [57] of the nonlocal van der Waals density functional (vdW-DF) theory of Dion et al. [58] was used to investigate the coupled bilayers. The more accurate, second version of the van der Waals density functional (vdW-DF2) theory of Lee et al. [59] was also used to study the coupling in these materials. In the vdW-DF2 scheme, an accurate refit [60] of the Perdew-Wang (PW86) semilocal exchange functional is used [61]. The Cooper exchange ($C09_x$) was originally proposed for describing the chemisorption of small molecules on layered systems [62]. We have also used the $C09_x$ exchange within the two vdW-DF schemes, i.e. vdW-DF$C09_x$ and vdW-DF2$C09_x$ functionals for comparative study.

Corrections to DFT, for long-range dispersive interactions, via semi-empirical atomic pairwise interactions are known [63,64] to give accurate description of large systems and molecular adsorption. Here, DFT-D2 and the more accurate DFT-D3 corrections have been applied within GGA-PBE to correct the effects of dispersive interactions on the electronic structure of the homogenous and heterogeneous bilayers. Within DFT-D2, the dispersion energy only includes pairwise additive correction$C_6^{ij}/r_{ij}^6$, evaluated as a sum over all pairs of atoms *i* and *j*. The $C_6$ correction scheme is semi-empirical in form, and the calculated dispersion coefficients are predetermined constant quantities that do not depend on the local chemical environment of interacting atoms *i* and *j*. Moreover, as the leading-term of the dispersion correction, these short-comings result in poor accuracy. The accuracy is further reduced because the scheme neglects many-body dispersion effects and faster decaying terms such as $C_8^{ij}/r_{ij}^8$ and $C_{10}^{ij}/r_{ij}^{10}$ interactions. Relative to experimental data, much improved accuracy of structural properties are obtained, at equilibrium interlayer separations, using the zero-damping D3 method (denoted here as PBE-D3) for comparison. In this PBE-D3 method, geometry-dependent dispersion coefficients were used, with default parameter settings for damping functions.

The electronic structures predicted within LDA(PZ) and GGA(PBE) approximations were confirmed in separate calculations with the Vienna *ab initio* simulation package (VASP) [65–68]. Because the large quasiparticle dynamics of graphene [69], also occurs in boronitrene [70,71], we performed fully self-consistent *GW* calculations to investigate the effect of quasiparticle corrections [72] on the size of the substrate-induced band gap [73]. In the VASP implementation, the fully self-consistent perturbative *GW* algorithm is used to update the wave functions and eigenvalues for calculating both the Green function *G* and screened Coulomb potential *W* contributions to the self-energy, starting from the GGA-PBE wave functions. The full shape of the GGA-PBE charge density was restored up to the maximum angular momentum of the *p*-electron states of C, Si, B and N atoms. The 4-iteration update calculations were performed on 24 (i.e. with 8 unoccupied) bands using 50 grid points for the determination of the frequency dependent components of the self-energy.

In all these calculations, the interaction between valence electrons and ion cores are described using projector-augmented wave (PAW) potentials [74]. Cut-off limits of 58 and 500 Ryd were set for kinetic energy and charge density expansion in the plane wave basis. It is relevant to note that the size of the unit cell used here ensures that the graphene overlayer always matches the underlying monolayer substrate with no reconstruction. Hence, the Brillouin zone sampling of electronic states was performed using the Monkhorst-Pack (MP) [75] grid of size $10 \times 10 \times 1$ for the isolated graphene and *h*-BN monolayers. Monolayer SiC substrate was modelled to be analogous to a single-atomic layer of the 6H-SiC in the $6\sqrt{3} \times 6\sqrt{3}$R30° superstructure. In the homogenous monolayer and bilayer structures, an $8 \times 8 \times 1$ mesh was sufficient to converge the interlayer distance and lattice parameter, independent of the XC functional. However, for coupled graphene/SiC heterobilayer systems, variable MP meshes, $m1 \times m2 \times 1$, were used to test for

convergence of physical properties. In this case, $m1$ and $m2$ determine the fineness of the MP mesh. The exact numbers used for $m1$ and $m2$ are shown in Table 1, and it is useful to state that convergence with respect to these two parameters have been established, and discussed in the following section. In each case, the total energy was converged to within $10^{-7}$ eV. In the self-consistent calculations of electronic energies, electron states were populated using the Methfessel–Paxton scheme [76], with a smearing width of 0.4 eV. All the supercells were optimized using the conjugate gradient algorithm with an atomic force convergence criterion of 0.01 eV/A. In each case, the bound graphene and monolayer substrates were modelled using a $1 \times 1$ periodic unit cell. The vacuum height was set to 15 A to avoid image interactions between periodically repeated cells.

## 3. Results and discussion

### 3.1. Accuracy of the k-point mesh on predicted structural properties

In Table 1, the accuracy of the $k$-point mesh was tested, in each case, on the structural properties of homogenous and heterogeneous systems. For graphite and bilayer graphene, the dependence of the lattice constant and inter-layer distance $h_0$ on XC functionals, and their comparison with experimental data, has already been published elsewhere [20], and will only be summarised here. As would be reasonably expected, the properties of the bilayer structures are generally similar to those of graphite. For example, although slightly smaller than the experimental value of 2.46 Å in both graphite and bilayer graphene [77], LDA predicts the same lattice constant (2.45 Å) for bilayer graphene and graphite. However, the LDA yields an equilibrium interlayer distance of 3.25 and 3.33 Å for graphite and bilayer graphene, respectively. Similarly, GGA-PBE predicts the same value of 4.10 Å for $h_0$, which overestimates the experimental value quite substantially. In each case, the two forms of non-local corrections (*i.e.* vdW-DF and vdW-DF2) yield the same values of 2.48 Å and 2.47 Å for graphite and bilayer graphene and the same interlayer distance of 3.5 Å. On the other hand, application of the semi-empirical correction to London-type dispersive interactions gives 3.28 and 3.09 Å (PBE-D2) and 3.34 and 3.36 Å (PBE-D3) for the equilibrium layer–layer separation in graphene and boronitrene bilayers. Both PBE-D2 and PBE-D3 correction schemes give the same lattice constant of 2.46 Å in graphene and bilayer graphene. Also, Table 1 shows that in similar homogenous bilayer systems, the calculated lattice constants of 2.51 Å ($h$-BN) and 3.084 Å (SiC) converge to their equivalent bulk values of 2.5047(2) Å [78], and 3.0810(2) Å [79], determined experimentally at room temperature.

The structural properties of graphite and hexagonal boron nitride are considerably similar. Therefore, the goal is to determine, as accurately as possible, the energy differences between well-converged graphene hetero-bilayer structures as they undergo transition to commensurability. It is essential therefore, that the associated energy differences be comparable to the error introduced by unconverged sampling of the Brillouin zone. Such errors are reduced as much as possible by using a very fine $k$-point mesh, without increasing the computational cost. It is noted here that $k$-point meshes centred at Γ gives faster convergence. Thus all $k$-points meshes used here were centred at Γ, but not all high symmetry points of the IBZ were included. For instance, the calculated energies converged slowly when the $k$-point mesh contains both the 'face centre', 'edges' and 'corners'. Also, odd $k$-point meshes gave poor convergence of total energies and lattice constants relative to even $k$-meshes, as expected. Table 1 also captures the effect of $k$-mesh on the heterogeneity of the graphene heterobilayer. In this case, lattice constant of the two heterobilayers are denoted as $a_{G-SiC}$ and $a_{G-BN}$ for comparison with lattice constants of homogenous bilayer structures (denoted as $a_{BN-BN}$, $a_{G-G}$, $a_{SiC-SiC}$). In all cases, it is found that the lattice constants are consistently well converged for calculations performed using $k$-point meshes of $m1 = m2 = 10$, irrespective of the nature of the bilayer. This implies that convergence of lattice constant with $k$-mesh is not sensitive to the intrinsic differences between the bilayer structures considered here. Thus, it is plausible to attribute this trend to the low lateral strain, and the absence of carbon segregation in the interfacial region between the graphene layer and the monolayer substrates. However, it is noted that the convergence point is shifted to a slightly higher mesh of $m1 = m2 = 15$ when odd $k$-point meshes are used.

**Table 1**
Equilibrium lattice constants for homogenous and heterogenous bilayers as a function of $k$-point mesh obtained using the vdw-DF scheme.

| $k$-Point mesh $m1 \times m2 \times 1$ | Lattice constant of bilayer structures (Å) | | | | |
|---|---|---|---|---|---|
| | $a_{SiC/SiC}$ | $a_{G/SiC}$ | $a_{BN-BN}$ | $a_{h-BN/G}$ | $a_{G/G}$ |
| $4 \times 4 \times 1$ | 3.074 | 3.076 | 2.46 | 2.46 | 2.38 |
| $6 \times 6 \times 1$ | 3.076 | 3.077 | 2.49 | 2.49 | 2.41 |
| $8 \times 8 \times 1$ | 3.081 | 3.083 | 2.53 | 2.52 | 2.44 |
| $10 \times 10 \times 1$ | 3.083 | 3.084 | 2.53 | 2.51 | 2.45 |
| $12 \times 12 \times 1$ | 3.082 | 3.085 | 2.52 | 2.50 | 2.46 |
| $14 \times 14 \times 1$ | 3.083 | 3.086 | 2.53 | 2.51 | 2.46 |
| $16 \times 16 \times 1$ | 3.081 | 3.086 | 2.52 | 2.52 | 2.46 |

### 3.2. Graphene adhesion to the heterogeneous monolayer

At ~2% persistent mismatch strain, the graphene lattice is commensurate on the $h$-BN monolayer [50]. Here, commensurability is achieved by periodic translation of the graphene C–C bonds over the substrate layer. Fig. 1a–f show equivalent stages in the translation of carbon bonds before the graphene becomes commensurate again with the substrate in the AA-stacking. The sequential translation from stages 1 to 6 corresponds to translational structures 1 → 2→3 → 4→5 → 6 before the translation from 6 to 1 gives commensurate graphene. Clearly, the atomic arrangements in stage 1 correspond to the simple (AA) stacking. In this case, the carbon atoms of the graphene layer are located directly above the atoms of the substrate, thus preserving the symmetry of the π-bonds. Because the position of carbon atoms in the graphene layer are skewed with respect to the substrate atoms, and the π-bonds are no longer aligned perpendicularly, thus breaking the symmetry of the π-bonds in each case in stages 2 (Fig. 1b), 4 (Fig. 1d) and 6 (Fig. 1f).

By contrast, the atomic arrangements in stages 3 and 5 show that the carbon atoms of graphene are arranged in the AB′- and A′B-Bernal stacking, respectively. In the AB′ (or A′B) stacking on $h$-BN substrate, the carbon atoms are arranged such that the boron (or nitrogen) atoms face the hollow sites of the graphene top layer. In the SiC substrate, the Si and C atoms of the SiC substrate face the hollow sites in AB′ and A′B stacking conformations respectively. By rescaling the lattice mismatch strain to 7.8%, the graphene top layer is equally made commensurate on SiC monolayer substrate. The total energy of the coupled bilayer structure of graphene on heterogeneous substrates was optimized with respect to the interlayer separation. Results are shown for graphene physisorption on monolayer substrates at stage 1 (AA stacking). This is because the other five stacking conformations identified as stages 2–6 yield relatively higher total energies at ground state. Next, we address the question of the functional dependence of the relative stabilities of the six identified stages in the C–C bond translation to commensurability at the equilibrium interlayer separation. The six

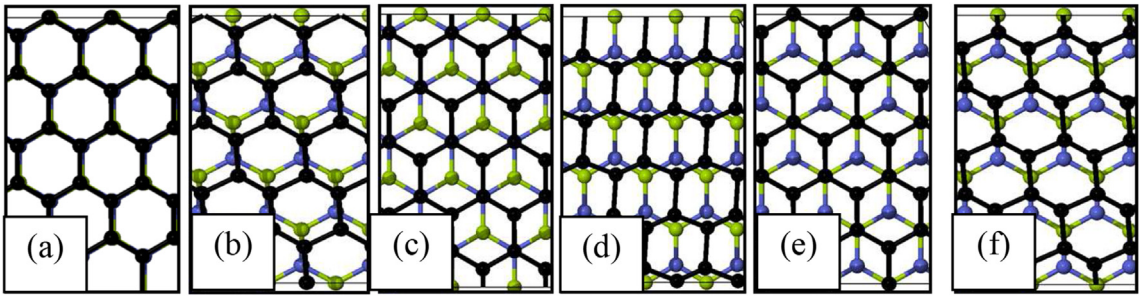


**Fig. 1.** Evolutionary stacking sequences in commensurate graphene on monolayer *h*-BN.

stages of the translation are denoted by Fig. 1a–f. For a given functional, offsets in energy is evaluated relative to the stage-index that presents the lowest total energy.

Fig. 2 shows the ground state total energy offset at the six translations to commensurability. In both SiC and *h*-BN, the use of Cooper exchange ($C09_x$) yields the same ground state total energy within the vdW-DFC09$_x$ and vdW-DF2C09$_x$ schemes. The energy offsets obtained from vdW-DFC09 and vdW-DF2C09 are substantially higher than those obtained using vdW-DF, vdW-DFC2, GGA and LDA approximations. All the functionals show that stage 4 is the most energetic bilayer structure. For graphene adsorbed on monolayer SiC, stage 6 gives a low energy structure, whereas it is relatively not stable when the graphene is physisorbed on *h*-BN. In both monolayer substrates, all the functionals predict stages 1, 2, 3 and 5 as competing low-energy structures consistently. The π-orbitals of the graphene carbon and the substrates atoms are misaligned in stages 2, 4 and 6. Also, only a third of the graphene carbon atoms undergo π-bonding with the substrate atoms in stages 3 and 5. Thus the discussion hereinafter focuses on the energetics and interlayer coupling of the AA-stacking order in stage 1 (see Fig. 1a). It is demonstrated that minimisation of the number and misalignment of π-bonds has nontrivial effects on the electronic structure, and opens a band gap at the Dirac ($KK'$) point.

Fig. 3 shows the dependence of the free energy on interlayer separation from different XC functionals. The energies are given as offsets relative to the total energy of the same structure, but at the largest interlayer separation (*i. e.* 8 Å). The lowest-energy structures of graphene on the SiC (Fig. 3a) and *h*-BN (Fig. 3b) monolayers show that equilibrium interlayer separation is sensitive to the approximations for the XC potential (see Table 2). Both LDA and GGA plots coincide at 5 Å (in SiC) and 4.5 (in *h*-BN) and both underestimate vdW interactions in the long range limit. For graphene physisorbed on SiC monolayer, the local (LDA) and semilocal (GGA) approximations predict considerably smaller interlayer distances compared to the vdW-DF functionals. Fig. 3a shows equilibrium interlayer distances of 2.61 Å (LDA) and 3.51 Å (GGA). These are shorter than the 3.77 Å predicted in each case, using vdW-DF and vdW-DF2 functionals. In similar multilayered materials, in which van der Waals forces dominate the interlayer coupling, the experimentally-determined interlayer distance is ~3.35 Å. When the Cooper exchange ($C09_x$) is used within the two vdW-DF schemes (i.e. vdW-DF C09 and vdW-DF2C09), the predicted interlayer coupling shows a considerable under-binding of the bilayer. The dependence of the equilibrium interlayer separation on the XC potentials gives 3.47 Å (LDA) and 3.90 Å (GGA), while vdW-DF and vdW-DF2 yield the same distance of 3.58 Å. Both vdW-DFC09 and vdW-DF2C09 schemes also give a large interlayer separation of 7.50 Å for SiC, and 6.5 Å for *h*-BN underlining the failure of the Cooper exchange in these systems.

Fig. 3b shows similar trends for variation in energy offsets with interlayer distance when graphene is physisorbed on the *h*-BN monolayer. All other functionals show vanishingly small difference in total energy between the coupled bilayers structures relative to their corresponding decoupled graphene on SiC and *h*-BN monolayers at the same distances of about 6.50 Å and 6.50 Å. Conversely, the LDA over binds them. It is relevant to add that the inclusion of dispersive London force corrections in the description of the equilibrium heterobilayer structures using PBE-D2 and PBE-D3 methods do not necessarily result in improved inter-layer separation $h_0$ in heterogeneous bilayer systems. For instance, within PBE-D2, $h_0$ is 4.36 and 4.04 Å for graphene on SiC and *h*-BN monolayers respectively. These reduce systematically to 3.52 Å and 3.32 Å within PBE-D3. Thus, corrections for van der Waals interactions within the PBE-D3 scheme yields the shortest interlayer distance, although the two non-local vdW-DF corrections give higher adhesion energies for the graphene overlayer on heterogeneous monolayer substrates. Consider that the interlayer distances predicted in Fig. 2 are generally higher than the distance (~3.35 Å) expected experimentally in similar, layered materials. Hence, incorporation of van der Waals interactions in the total energy functional does not necessarily improve the interlayer coupling. Hence, we suggest that the adhesion energy of the bilayer systems can give better insights to the interlayer coupling. Besides, it is important in describing the properties of the interfacial region between the two bound monolayers.

To determine, theoretically, which of the stacking configurations in Fig. 1 gives the most stable interface, it is crucial to first establish feasible models on the basis of the distinct stacking sequences, and then compare them. It is noted however, that the direct comparison of the total energies of such stacking models is not physically meaningful since the interfaces may contain different number of atoms. Alternatively, the adhesion energy ($E_{adh}$) [80,81] is physically intuitive for the prediction of the mechanical properties of an interface, and is directly comparable for interfaces that contain different number of atoms. In this case, adhesion energy is the reversible energy required to decouple the bilayer structure into freestanding monolayers. The adhesion energy was calculated as the difference in total energy between the coupled layer and the isolated single layers as $E_{adh} = [E(gr) + E(sub) - E(coupled)]$, where $E(coupled)$ is the total energy of the supercell of coupled graphene monolayer substrates in the lowest energy (i.e. equilibrium) structure. The terms $E(gr)$ and $E(sub)$ denote the total energies of the free-standing monolayers of graphene and SiC. The adhesion energy gives an indication of the tendency of graphene to stick to the monolayer substrates in typical heterojunctions, and therefore the stability of the coupled bilayers.

From all the functionals, the adhesion energy is highest in stage 1 and lowest in stage 4. It is intuitive to ascribe this trend to the complete alignment of π-orbitals in stage 1 to give maximum overlap. By contrast, π-orbital alignment in stages 2, 4 and 6 give the least overlap. Table 2 shows the functional dependence of the adhesion energies in stage 1 (Fig. 1). The two vdW-DF functionals

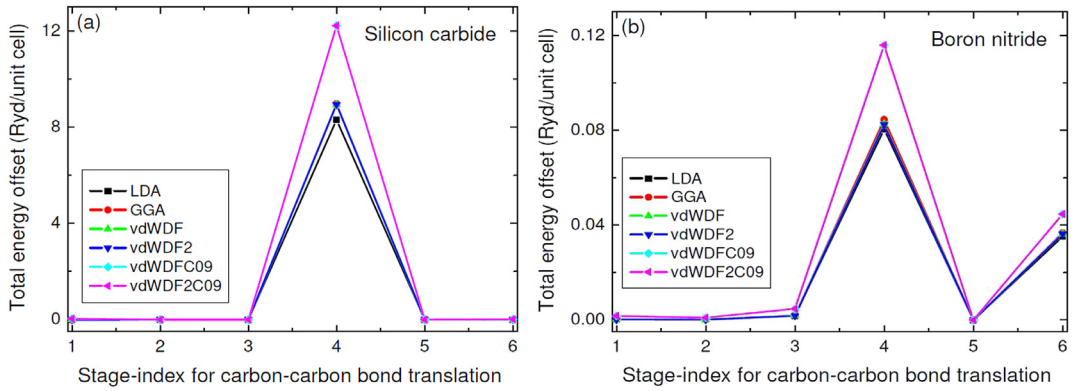


**Fig. 2.** Differences in total energy at the ground state in the six-stages identified for the translation of carbon–carbon bonds to achieve commensurability of graphene on silicon carbide (a) and boron nitride (b) monolayers.

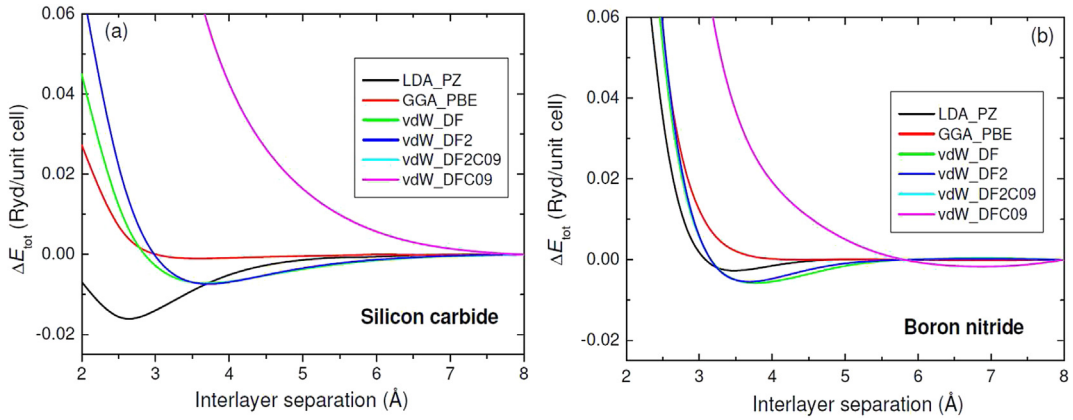


**Fig. 3.** Free energy of coupled heterobilayers of stage 1 conformation graphene on silicon carbide (a) and hexagonal boron nitride (b).

show a stronger adhesion of graphene on SiC in contrast to the *h*-BN. Conversely, Cooper exchange-corrections yield the opposing trend. The LDA adhesion energy is significantly higher for the coupling of graphene on SiC than on *h*-BN monolayer. Apart from the vdW-DFC09 and vdW-DF2C09, both LDA and GGA give the weakest coupling of graphene on the *h*-BN monolayer, while vdW-DF and vdW-DF2 give the strongest coupling. The trends in interlayer coupling can be understood from the viewpoint of variations in electron density in the bilayer structure. Because local electron density is non-homogeneous within the bilayers, graphene adhesion is hard to describe properly within the local (LDA) and semi-local (GGA) approximations. However, both vdW-DF and vdW-DF2 give consistent trends in $E_{ads}$ to suggest the stability of bound graphene/monolayer substrates from SiC and *h*-BN.

In order to compare the predicted structural properties of the graphene/SiC heterobilayer with published data, it is important to note that in modelling the growth of epitaxial graphene on either Si-terminated [41–43] or C-terminated [44–46] faces of 6H:SiC(0001) substrate using lateral supercells, the buffer carbon layer behaves differently to the cases considered here. Firstly, this difference is attributed to the facts that the C- and Si-terminated faces of the 6H:SiC substrate retain their bulk structures, and can absorb the lateral strain expected during the coupling of the first graphene *buffer* layer. For instance, using empirical interatomic potentials, Lampin et al. [82] found that the C atoms in the graphene buffer layer are located at distances within 2.1–2.2 Å from the surface with surface C coupled at different strengths. In this case, some of the carbon coupled strongly to, while the remaining carbon atoms are completely disconnected from, the surface. Using DFT calculations, Sclauzero and Pasquarello [83] also found that the average graphene/SiC separation is 2.26–2.28 Å. Consider that the trend in these two different types of calculations is consistent, and shows that graphene couples to bulk SiC substrates at distances that are far lower than the interlayer spacing (3.35 Å) in graphite, irrespective of the periodicity of the graphene superlattice. Secondly and more importantly, the long coupling distances (see Table 2), between the graphene overlayer and heterogeneous monolayers compared to bulk substrates suggest that it is the interface geometry, and not the intrinsic polarity of the monolayer, that controls the coupling dynamics in van der Waals heterobilayers.

### 3.3. Formation of interface dipole from localised inhomogeneities

Fig. 4 shows the contour maps of difference charge density distribution along the transverse section of the bilayer structure, plotted on the same scale, in physisorbed graphene on SiC and *h*-BN monolayer. In the top and bottom layers of both structures, colour contrasts of the contour maps show localised charge densities mainly along C–C, Si–C and B–N bonds. Along the plane of the SiC monolayer substrate, a significantly lower charge density is observed at the Si site, as opposed to the C site. Similarly, the N site of the *h*-BN monolayer is also characterised by a lower charge density relative to the B-site. Nevertheless, comparisons of the two monolayer substrates show that the charge density at the Si site is significantly lower that the charge density obtained at the N-site.

**Table 2**
XC functional dependence of the equilibrium interlayer spacing (in Å) and adhesion energy (in mRyd/cell) for graphene on SiC and *h*-BN monolayers under stage 1 stacking.

| Functional | SiC | | *h*-BN | |
|---|---|---|---|---|
| | $E_{ads}$ | $h_0$ | $E_{ads}$ | $h_0$ |
| vdW-DF | 7.40 | 3.77 | 5.68 | 3.58 |
| vdW-DF2 | 7.40 | 3.77 | 5.68 | 3.58 |
| vdW-DFC09 | 0.14 | 7.50 | 1.78 | 6.5 |
| vdW-DF2C09 | 0.14 | 7.50 | 1.78 | 6.5 |
| LDA | 15.67 | 2.61 | 2.77 | 3.47 |
| GGA-PBE | 1.07 | 3.43 | 0.14 | 3.90 |
| PBE-D2 | 5.88 | 4.36 | 2.81 | 4.04 |
| PBE-D3 | 5.51 | 3.52 | 2.66 | 3.32 |

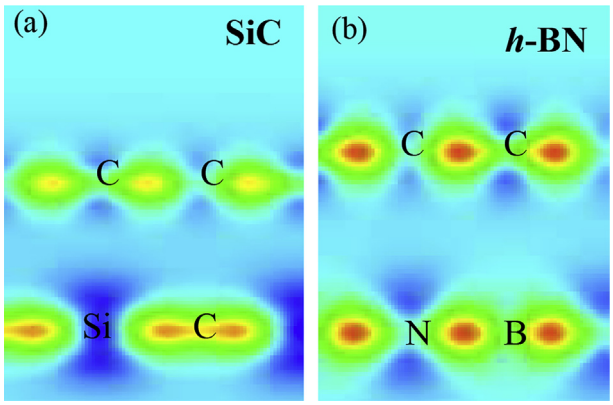


**Fig. 4.** Contour maps of the difference charge density for physisorbed graphene on SiC (a) and *h*-BN (b) monolayers along the transverse section of the heterobilayer structure.

The magnitude of the charge density between neighbouring carbon atoms of the top layers, though similar, are non-uniform. The charge density is localised mainly on the carbon–carbon bond-centres, although the charge density along the carbon bond centres of the two graphene top layers are slightly different.

Fig. 4a shows that when graphene is overlaid on SiC, the electronic density is weakly localised at the carbon bond centres compared to the stronger localisation observed when graphene is physisorbed on *h*-BN (Fig. 4b). Despite of similarities in the distribution of the *in-plane* charge density in the two bilayers, we show that the differences observed in the site-resolved *in-plane* charge densities have profound consequences on the electronic structure that culminates in the formation of charge puddles in the graphene/substrate interface and interfacial dipoles. Assume that the charge density on the top ($\rho_t$) and bottom ($\rho_b$) layers are nonzero. From charge-neutrality requirements, static transverse electric field is expected to develop within the interface region. Thus, the difference $\Delta\rho$ between the top ($\rho_t$) and bottom ($\rho_b$) layer densities must be infinitesimally small but nonzero for a static, non-vanishing, interfacial electric field to form. Otherwise, a vanishing difference charge density $\Delta\rho$corresponds to zero interfacial electric field, and denotes zero total potential between the two layers. We demonstrate, in the following, that the interface electric field is finite because the total local potential is nonzero within the region between the two monolayers.

The interface structure of van der Waals heterostructure plays an important role in heterojunction device applications. The variations in the macroscopic average potential are integrated along the shortest interlayer distance between bound monolayers, in each case. Although the total local potential exhibits different characteristic in both heterostructures, both vdW-DF approximations yield similar TLP profiles. Absolute differences in the datasets are less than $10^{-8}$ V per structure. It is found that a negative (graphene/SiC) and positive (graphene/h-BN) potential is set up in the interface. Only marginal increases are observed in the TLP within 1.0 Å away from the *h*-BN monolayer. However, there is a sharp monotonic increase to its peak potential at 2 Å below the graphene over-layer. Beyond 2 Å, and up to 2.5 Å, the TLP shows decays exponentially but remain unchanged up to the graphene layer. We obtain an interfacial electric field of 192 mVÅ$^{-1}$, derived as the negative gradient of the extremal potential difference measured at the SiC (−9.62 V) and graphene (−5.83 V) monolayers.

Positive potentials of the graphene/*h*-BN system are 1.94 V (top layer) and 2.63 V (bottom layer), which corresponds to an interface electric field of −1053 mVÅ$^{-1}$. It is relevant to note that the electric field vector points in reverse direction. The polarity of the interface electric field though reversed, has considerably stronger intensity. Both cases suggest the formation of interface dipole with substrate dependent electric field polarity. Differences in polarities of the interfacial electric field suggest that the net charge imbalance between the top and bottom layers is by charge-donating impurities below the graphene overlayer. In such van der Waals bilayer heterostructures, this imbalance arises from the coupling of electron–electron interactions even when there is no inter-layer exchange of carriers. The coupling influences the transfer of momentum between electron and hole states such that the resultant imbalance in carrier density causes considerable Coulomb drag at short inter-particle separations [84].

### 3.4. Anisotropy-induced band gap

Fig. 5 shows quasiparticle-corrected band structures within the range $-4 \leq E(\text{eV}) \leq 4$ in the vicinity of the *KK*′-point. Here, only *extremum* band gaps are shown for graphene on SiC (bottom panels), and on *h*-BN (top panels) monolayers. The stage indices in Fig. 5 correspond to heterobilayer stacking configurations with maximal (smallest) or minimal (largest) band gaps. These show that the band gap is substantially dependent on the stacking order. The possibility of obtaining a spontaneous band gap in graphene through the modification of the growth orientation on *h*-BN monolayer has also been observed in tight binding (TB) calculations [85]. The vdW-DF and *GW* calculations presented here confirms the shifts in Dirac point energy due to incommensurability. In stages 4 and 6, the IBZ shows small shifts in the direction from point K to point M. This indicates clearly that the disorder in the heterogeneous monolayer plays a role in inducing the band gap in graphene when the bilayer has the correct stacking sequence. This observed agreement between two different types of calculations alludes to similarities in the mechanism of the anisotropy-induced *KK*′-point band gap. The *KK*′ point band gap is therefore not an artefact of calculation, but must have a deeper fundamental origin, that is possibly related to the overlap between $\pi$-orbitals within the interlace region. In Fig. 5, the energy dispersion shows four (three) closely-spaced bands within the range of ±4 eV, for graphene on *h*-BN (SiC) monolayer. These suggest that the substrate effect on the band structure is strong, or at least nontrivial.

Thus, the interaction of the substrate with the graphene overlayer causes significant band repulsion between electron states localised within the two top-lying valence and low-lying conduction bands. The strength of these repulsive interactions must therefore be sensitive to the stacking sequence. In GNRs, this effect is observable as the Coulomb blockade at zero bias [86,87]. Because analogous TB calculations using substrate-induced mass terms give fundamentally similar conclusions, we conclude that varying the graphene/substrate stacking sequence under persistent mismatch

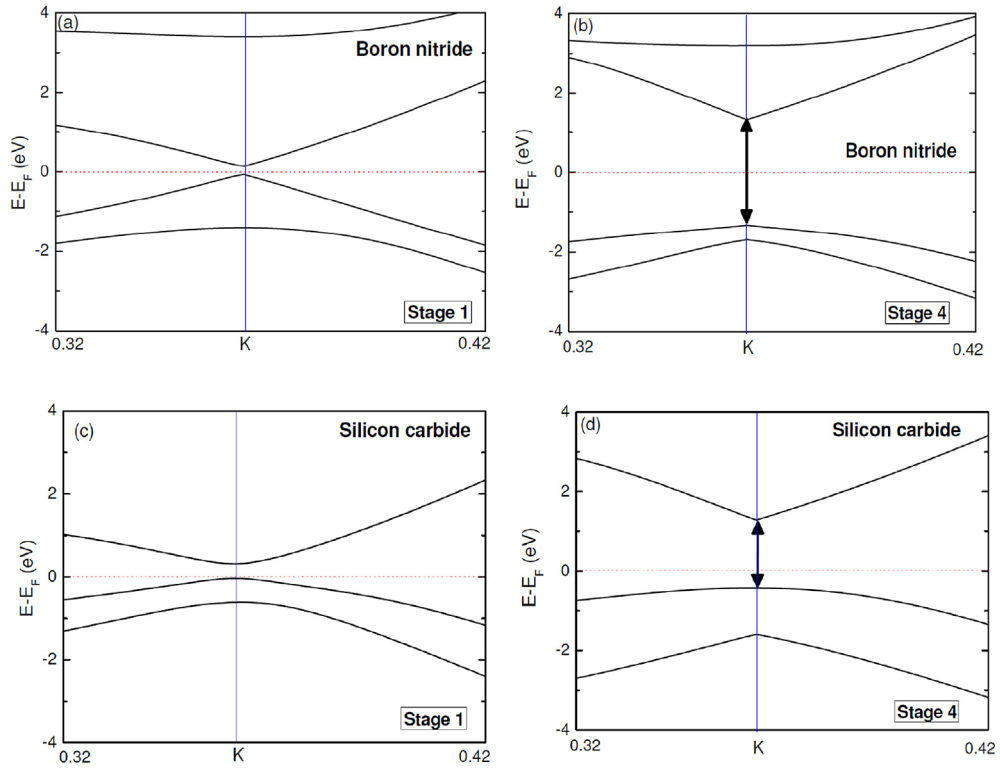


**Fig. 5.** Minimum and maximum band gaps in quasiparticle-corrected *E-k* dispersions around the Dirac point in heterobilayers of graphene on *h*-BN (top panels), and SiC (bottom panels).

strain yields a variable band gap at the *KK′*-point. In both substrates, the *KK′*-point band gap varies sinusoidally with the sequential stacking order denoted by the stage index. For graphene on *h*-BN monolayer, *KK′*-point gaps of 0.22 eV (stage 1), 1.04 eV (stage 2), 0.06 eV (stage 3) 2.69 eV (stage 4), 0.20 eV (stage 5) and 1.78 eV (stage 6) are obtained. We emphasize however, that the electronic structure of the fully-sampled IBZ shows band crossings along the A → Γ → M directions in stage 4 and along M → K → Γ direction in stage 2. Hence, there is no effective band gap when the stacking order corresponds to stage 4, and the resulting electronic structure has metallic character.

In the semiconducting state, the smallest (and largest) band gap occurs in stage 3 (and stage 6) of both substrates. The largest band gap for graphene on silicon carbide monolayer is 1.13 eV. This is 0.65 eV smaller than the band gap of 1.78 eV obtained for graphene on the *h*-BN monolayer. It is relevant to recall from Fig. 2 that the stage 1 in both substrates gives a far lower energy offsets compared to stage 4. Hence, the stacking in stage 4 does not result in a competing low-energy structure. The energy offset of stage 4 is always higher than the corresponding offset in all other stages by at least 8 Ryd/unit cell in SiC and 0.12 Ryd/unit cell. We note that the free energy of all the structures is negative; hence their spontaneous formation is distinctly possible. Thus, conventional methods of graphene synthesis may not yield a spontaneous band gap at ground state. However, the possibility of obtaining it by CVD growth process engineering to obtain the skewed atomic arrangement in stage 4 or during the post-synthetic docking of the graphene layer on the substrate cannot be overruled.

Differences in localisation of the charge density and the dependence of the interlayer potential difference on disorder potential shows spatial variations in magnitude and polarity of the interfacial electric field (see Fig. 4) in agreement with Rutter et al. [88]. Thus the potential difference between the top and bottom layers of bilayer graphene is directly proportional to the charge imbalance, and the magnitude of this potential difference determines the size of the band gap. It is plausible that the structural anisotropy in the heterobilayer breaks the symmetry of pristine bilayer graphene in each cases leading to formation of charge puddles and interfacial electric fields due to microscopic polarisation. By maintaining minimal overlap interactions between π-orbitals of the heterobilayer, a band gap opens up at the Dirac point relative to pristine graphene bilayer. The influence the anisotropy on the electronic structure of the graphene layer can be understood from the viewpoint of how closely packed the electron states are distributed under persistent strain in the different planar stacking conformations. Hence, the electronic density of states (DOS) is investigated within the vdW-DF2 scheme, and characteristic spectral features are identified to further unravel the origin of the band gap.

Fig. 6 shows the corresponding quasiparticle-corrected DOS of the graphene overlayer on monolayers of *h*-BN and SiC in stage 3 (top panels) and stage 6 (bottom panels), respectively. For comparison, the total DOS is shown as combined plots, in each case, with the DOS of pristine bilayer graphene. However, the bilayer graphene structure is stacked to correspond to stage 6 conformation [see Fig. 1f]. Despite the persistent strain, the structure of bilayer graphene is isotropic because the local electronic density is homogenous. In both monolayer substrates, the electronic structure exhibits the semiconducting transport characteristics. The DOS profiles exhibit sharp 'kinks' (i.e. discontinuities) in the distribution of electronic states. These kinks are van Hove singularities, and they occur at critical points of the IBZ. With the Fermi level ($E_F$) always aligned to correspond to the 0 = eV energy level, Fig. 6b and d shows a sharp discontinuity at the top of the valance band, just below the Fermi level ($E_F$) for the SiC substrate.

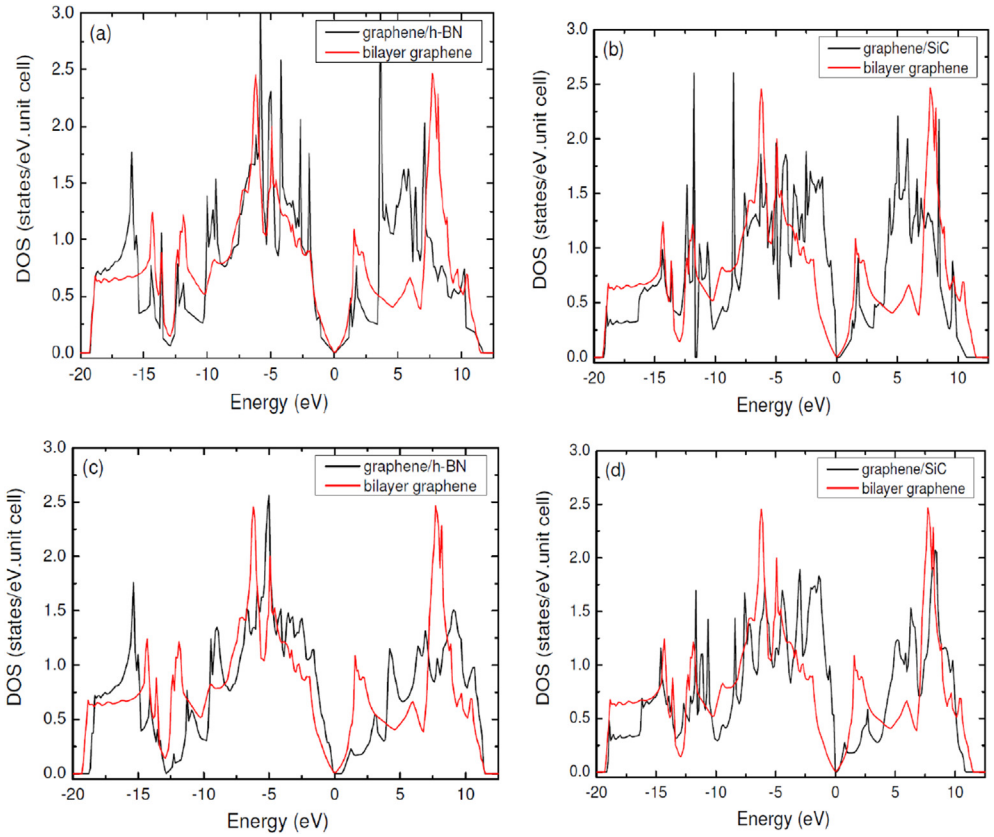


**Fig. 6.** Electronic DOS in heterobilayers superimposed on bilayer graphene DOS to show maximal (top panels) and minimal (bottom panels) band gaps.

The electronic DOS shows no spectral gaps in the electronic structure despite the prominent presence of van Hove singularities. Due to the relatively high persistent strain, spectral splitting of either the conduction or valence band would have been expected when graphene is overlaid on the SiC monolayer [89,90]. However, a sharp discontinuity occurs just below 12.5 eV [see Fig. 6b] within the valence band (VB) when the structure has lowest band gap. Although the discontinuity persists in the graphene/SiC structure when the band gap is maximum, there is a non-zero DOS at the corresponding energy level. Fig. 6a and c shows that the *h*-BN monolayer causes considerable splitting of VB states just above 12.5 eV. In the maximum band gap structure, there is no discontinuity in occupied electronic states at the same mismatch strain. This suggests that interplay exist between the substrate anisotropy, the van Hove singularity, and the induced band gap. Fig. 6a and c shows an exponential decay dependence of VB edge states within the energy interval $-2.5 < E(\text{eV}) < 0$. This directly contrasts with the linear dependence of similar edge states in Fig. 6b and d. Comparisons of Fig. 6a–6d with pristine bilayer graphene DOS, allows for isolation of the electronic signatures of the structural anisotropy, particularly around the Fermi level. Firstly, there is nearly a one-to-one matching between states at the top of the valence band in pristine bilayer graphene and those in the heterogeneous bilayers, when the band gap is minimal (see Fig. 6a). Slightly higher population of electronic states is observed at the top of the valence band edge relative to the corresponding pristine bilayer graphene structure, when the band gap is maximum (Fig. 6c).

It is plausible that the delicate interplay between the minimisation of the misalignment between the interlayer π-bonds is responsible for opening up the band gap. A large offset is observed in graphene/SiC VB states relative to the bilayer graphene. This appears in Fig. 6b and d as a sharp reduction in the density at the top of the VB. This effect is akin to van Hove singularities close to the Fermi level, and should have non-trivial effects on the resulting band gap. The resultant band-splitting of the singularities culminates in the opening of the spontaneous band gap in the bilayer structure. This nontrivial effect has been probed by decomposing the DOS into atom-specific angular momentum contributions in the heterobilayer structures whose stacking sequence yields the highest band gap. It is found that the density of *s*-electron states is smaller than the density of *p*-electron states by an order of magnitude. The sharp discontinuity observed around the position of the Fermi level i.e. $E = 0$ eV, is traced to the effects of the sublattice atoms of the SiC unit cell. Unlike the *h*-BN monolayer where the effect is reduced substantially, Si and C *p*-state DOS suggest that atoms of the SiC monolayer substrate are the primary source of van Hove singularity at the Fermi level.

## 4. Conclusions

In this paper, a comparative density functional study of the bilayer heterostructure derived from the coupling of graphene/SiC, and graphene/hexagonal BN monolayers has been presented. The local, semi-local, and semi-empirical van der Waals energy-corrected density functional theory has been used to show that the energy required for graphene adhesion on SiC (7.4 eV) and *h*-BN (5.68 eV) is invariant under non-local dispersion corrections. Semi-empirical corrections for van der Waals interactions within the PBE-D3 scheme yields the shortest interlayer distance in graphene heterobilayers, whereas the two non-local corrections (*i.e.* vdW-DF and vdW-DF2) give higher adhesion energies. However, the Cooper

exchange functional (C09x) when used in non-local correction schemes results in considerable underbinding of the bilayer heterostructures. It is found that the structural evolution of heterobilayers under persistent strain induces localised charge puddles in the electronic structure. The origin of the spontaneous zero-field band gap in the graphene overlayer on lattice mismatched monolayers has been investigated to show its tunability by varying the stacking sequence. Using the differences between the electronic structure of pristine graphene bilayer and graphene heterobilayers, it is argued that the formation of interface dipoles is ascribable to the strain induced by the structural anisotropy at persistent lattice mismatch between the layers. This structural anisotropy breaks the symmetry of pristine bilayer graphene in the two cases considered, suggesting that the bilayer coupling must maintain minimal overlap between the $\pi$-orbitals and minimize their interactions in order to open the Dirac point band gap. Nevertheless, the band gap within the *s*-electron DOS is a wide, and does not change rapidly from −2.5 eV up to the Fermi level. On the other hand, the occupied *p*-electron states decay off exponentially into the band gap without any kinks, and therefore no van Hove singularities up to the Fermi level. It is concluded that spontaneous band gap can opens in the electronic structure by modifying the growth orientation of the graphene overlayer on monolayer substrates. In each case, the induced band gaps are 1.13 and 1.78 eV at the Dirac ($KK'$) point, for graphene on silicon carbide and hexagonal boron nitride monolayers. Our results suggest that the effect of microscopic mechanisms such as band repulsion and interface dipole formation are crucial to the formation of the band gap in supported graphene layers.

## References


[1] K.S. Novoselov, A.K. Geim, S.V. Morozov, D. Jiang, Y. Zhang, S.V. Dubonos, I.V. Grigorieva, A.A. Firsov, Electric field effect in atomically thin carbon films, Science 306 (2004) 666.
[2] F. Schwierz, Graphene transistors, Nat. Nanotechnol. 5 (2010) 487.
[3] A.K. Geim, I.V. Grigorieva, Van der Waals heterostructures, Nature 499 (2013) 419–425.
[4] Y. Sakai, S. Saito, M.L. Cohen, Lattice matching and electronic structure of finite-layer graphene/*h*-BN thin films, Phys. Rev. B 89 (2014) 115424.
[5] X. Zhong, R.G. Amorim, R.H. Scheicher, R. Pandey, S.P. Karna, Electronic structure and quantum transport properties of trilayers formed from graphene and boron nitride, Nanoscale 4 (2012) 5490.
[6] A. Hashmi, J. Hong, Band gap and effective mass of multilayer BN/graphene/BN: van der Waals density functional approach, Appl. Phys. 115 (2014) 194304.
[7] W. Hu, Z. Li, J. Yang, Structural, electronic, and optical properties of hybrid silicene and graphene nanocomposite, J. Chem. Phys. 139 (2013) 154704.
[8] N. Gao, J.C. Li, Q. Jiang, Tunable band gaps in silicene-$MoS_2$ heterobilayers, Phys. Chem. Chem. Phys. 16 (2014) 11673.
[9] M. Ishigami, J.H. Chen, W.G. Cullen, M.S. Fuhrer, E.D. Williams, Atomic structure of graphene on $SiO_2$, Nano Lett. 7 (2007) 1643.
[10] E. Stolyarova, K.T. Rim, S. Ryu, J. Maultzsch, P. Kim, L.E. Brus, T.F. Heinz, M.S. Hybertsen, G.W. Flynn, High-resolution scanning tunneling microscopy imaging of mesoscopic graphene sheets on an insulating surface, Proc. Natl. Acad. Sci. 104 (2007) 9209.
[11] V. Geringer, M. Liebmann, T. Echtermeyer, S. Runte, M. Schmidt, R. Ruchamp, M.C. Lemme, M. Morgenstern, Intrinsic and extrinsic corrugation of monolayer graphene deposited on $SiO_2$, Phys. Rev. Lett. 102 (2009) 076102.
[12] Z.H. Aitken, R. Huang, Effects of mismatch strain and substrate surface corrugation on morphology of supported monolayer graphene, J. Appl. Phys. 107 (2010) 123531.
[13] Y. Zhang, V.W. Brar, C. Girit, A. Zettl, M.F. Crommie, Origin of spatial charge inhomogeneity in graphene, Nat. Phys. 5 (2009) 722.
[14] R. Decker, Y. Wang, V.W. Brar, W. Regan, H.-Z. Tsai, Q. Wu, W. Gannett, A. Zettl, M.F. Crommie, Local electronic properties of graphene on a BN substrate via scanning tunneling microscopy, Nano Lett. 11 (2011) 2291.
[15] S. Adam, E.H. Hwang, V.M. Galitski, S. Das Sarma, A self-consistent theory for graphene transport, Proc. Natl. Acad. Sci. 104 (2007) 18392.
[16] J. Martin, N. Akerman, G. Ulbrich, T. Lohmann, J.H. Smet, K. Von Klitzing, A. Yacoby, Observation of electron-hole puddles in graphene using a scanning single-electron transistor, Nat. Phys. 4 (2008) 145.
[17] L.L. Song, X.H. Zheng, R.L. Wang, Z. Zeng, Dangling bond states, edge magnetism, and edge reconstruction in pristine and B/N-terminated zigzag graphene nanoribbons, J. Phys. Chem. C 114 (2010) 12145.
[18] Z. Liu, K. Suenaga, P.J.F. Harris, S. Iijima, Open and closed edges of graphene layers, Phys. Rev. Lett. 102 (2009) 015501.
[19] Y. Ma, Y. Dai, M. Guo, C. Niu, L. Yu, B. Hunag, Strain-induced magnetic transitions in half-fluorinated single layers of BN, GaN and graphene, Nanoscale 3 (2011) 2301.
[20] R.E. Mapasha, A.M. Ukpong, N. Chetty, Ab initio studies of hydrogen adatoms on bilayer graphene, Phys. Rev. B 85 (2012) 205402.
[21] G. Gui, J. Li, J. Zhong, Band structure engineering of graphene by strain: first-principles calculations, Phys. Rev. B 78 (2008) 075435.
[22] G. Cocco, E. Cadelano, L. Colombo, Gap opening in graphene by shear strain, Phys. Rev. B 81 (2010) 241412.
[23] L. Yang, C.H. Park, Y.W. Son, M.L. Cohen, S.G. Louie, Quasiparticle energies and band gaps in graphene nanoribbons, Phys. Rev. Lett. 99 (2007) 186801.
[24] M.Y. Han, B. Özyilmaz, Y.B. Zhang, P. Kim, Energy band-gap engineering of graphene nanoribbons, Phys. Rev. Lett. 98 (2007) 206805.
[25] X. Li, X. Wang, L. Zhang, S. Lee, H. Dai, Chemically derived, ultrasmooth graphene nanoribbon semiconductors, Science 319 (2008) 1229.
[26] Z. Chen, Y.M. Lin, M.J. Rooks, P. Avouris, Graphene nano-ribbon electronics, Phys. E 40 (2007) 228.
[27] M. Batzill, The surface science of graphene: metal interfaces, CVD synthesis, nanoribbons, chemical modifications, and defects, Surf. Sci. Rep. 67 (2012) 83.
[28] R. He, L. Zhao, N. Petrone, K.S. Kim, M. Roth, J. Hone, P. Kim, A. Pasupathy, A. Pinczuk, Large physisorption strain in chemical vapor deposition of graphene on copper substrates, Nano Lett. 12 (2012) 2408.
[29] L. Gao, J.R. Guest, N.P. Guisinger, Epitaxial graphene on Cu(111), Nano Lett. 10 (2010) 3512.
[30] J. Coraux, A.T. N'Diaye, M. Engler, C. Busse, D. Wall, N. Buckanie, F. Heringdorf, R. van Gastei, B. Poelsema, T. Michely, Growth of graphene on Ir(111), New J. Phys. 11 (2009) 023006.
[31] E. Sutter, P. Albrecht, P. Sutter, Graphene growth on polycrystalline Ru thin films, Appl. Phys. Lett. 95 (2009) 133109.
[32] J. Wintterlin, M.L. Bocquet, Graphene on metal surfaces, Surf. Sci. 603 (2009) 1841.
[33] K.S. Novoselov, D. Jiang, F. Schedin, T.J. Booth, T.T. Khotkevich, S.V. Morozov, A.K. Geim, Two-dimensional atomic crystals, Proc. Natl. Acad. Sci. 102 (2005) 10451.
[34] C.R. Dean, A.F. Young, I. Meric, C. Lee, L. Wang, S. Sorgenfrei, K. Watanabe, T. Taniguchi, P. Kim, K.L. Shepard, J. Hone, Boron nitride substrates for high-quality graphene electronics, Nat. Nanotechnol. 5 (2010) 722.
[35] C. Lee, Q. Li, W. Kalb, X.-Z. Liu, H. Berger, R.W. Carpick, J. Hone, Frictional characteristics of atomically thin sheets, Science 328 (2010) 76.
[36] J. Xue, J. Sanchez-Yamagishi, D. Bulmash, P. Jacquod, A. Deshpande, K. Watanabe, T. Taniguchi, P. Jarillo-Herrero, B. LeRoy, Scanning tunnelling microscopy and spectroscopy of ultra-flat graphene on hexagonal boron nitride, Nat. Mater. 10 (2011) 282.
[37] C. Dean, A.F. Young, L. Wang, I. Meric, G.-H. Lee, K. Watanabe, T. Taniguchi, K. Shepard, P. Kim, J. Hone, Graphene based heterostructures, Solid State Commun. 152 (2012) 1275.
[38] W. Gannett, W. Regan, K. Watanabe, T. Taniguchi, M.F. Crommie, A. Zettl, Boron nitride substrates for high mobility chemical vapor deposited graphene, Appl. Phys. Lett. 98 (2011) 242105.
[39] R.V. Gorbachev, I. Riaz, R.R. Nair, R. Jalil, L. Britnell, B.D. Belle, E.W. Hill, K.S. Novoselov, K. Watanabe, T. Taniguchi, A.K. Geim, P. Blake, Hunting for monolayer boron nitride: optical and Raman signatures, Small 7 (2011) 465.
[40] P. Vogt, P. De Padova, C. Quaresima, J. Avila, E. Frantzeskakis, M.C. Asensio, A. Resta, B. Ealet, G. Le Lay, Silicene: compelling experimental evidence for graphene like two-dimensional silicon, Phys. Rev. Lett. 108 (2012) 155501.
[41] C. Virojanadara, M. Syväjärvi, R. Yakimova, L.I. Johansson, A.A. Zakharov, T. Balasubramanian, Homogeneous large-area graphene layer growth on 6H-SiC(0001), Phys. Rev. B 78 (2008) 245403.
[42] C. Virojanadara, R. Yakimova, J.R. Osiecki, M. Syväjärvi, R.I.G. Uhrberg, L.I. Johansson, A.A. Zakharov, Substrate orientation: a way towards higher quality monolayer graphene growth on 6H-SiC(0001), Surf. Sci. Lett. 603 (2009) L87.
[43] C. Virojanadara, R. Yakimova, A.A. Zakharov, L.I. Johansson, Large homogeneous mono-/Bi-layer graphene on 6H-SiC(0001) and buffer layer elimination, J. Phys. D Appl. Phys. 43 (2010) 374010.
[44] J.K. Hite, M.E. Twigg, J.L. Tedesco, A.L. Friedman, R.L. Myers-Ward, C.R. Eddy, D.K. Gaskill, Epitaxial graphene nucleation on C-face silicon carbide, Nano Lett. 11 (2011) 1190.
[45] J.L. Tedesco, G.G. Jernigan, J.C. Culbertson, J.K. Hite, Y. Yang, K.M. Daniels, R.L. Myers-Ward, C.R. Eddy, J.A. Robinson, K.A. Trumbull, M.T. Wetherington, P.M. Campbell, D.K. Gaskill, Morphology characterization of argon-mediated epitaxial graphene on C-face SiC, Appl. Phys. Lett. 96 (2010) 222103.
[46] W.A. de Heer, C. Berger, M. Ruan, M. Sprinkle, X. Li, Y. Hu, B. Zhang, J. Hankinson, E. Conrad, Large area and structured epitaxial graphene produced by confinement controlled sublimation of silicon carbide, Proc. Natl. Acad. Sci. 108 (2011) 16900.
[47] X. He, T. He, Z. Wang, M. Zhao, Phys. E 42 (2010) 2451.
[48] E. Bekaroglu, M. Topsakal, S. Cahangirov, S. Ciraci, Phys. Rev. B 81 (2010) 075433.
[49] K.S. Novoselov, D. Jiang, F. Schedin, T.J. Booth, T.T. Khotkevich, S.V. Morozov, K. Geim, Proc. Natl. Acad. Sci. U. S. A. 192 (2005) 30.
[50] X. Zhao, L. Li, M. Zhao, Lattice match and lattice mismatch models of graphene on hexagonal boron nitride from first principles, J. Phys. Condens. Matter 26 (2014) 095002.

[51] E. Kim, N. Jain, R. Jacobs-Gedrim, Y. Xu, B. Yu, Exploring carrier transport phenomena in CVD-assembled graphene FET on hexagonal boron nitride, Nanotechnology 23 (2012) 125706.
[52] G.H. Lee, Y.J. Yu, C. Lee, C. Dean, K.L. Shepard, P. Kim, J. Hone, Electron tunnelling through atomically flat and ultrathin hexagonal boron nitride, Appl. Phys. Lett. 99 (2011) 243114.
[53] C.R. Woods, L. Britnell, A. Eckmann, R.S. Ma, J.C. Lu, H.M. Guo, X. Lin, G.L. Yu, Y. Cao, R.V. Gorbachev, A.V. Kretinin, J. Park, L.A. Ponomarenko, M.I. Katsnelson, Y.N. Gornostyrev, K. Watanabe, T. Taniguchi, C. Casiraghi, H.-J. Gao, A.K. Geim, K.S. Novoselov, Commensurate–incommensurate transition in graphene on hexagonal boron nitride, Nat. Phys. 10 (2014) 451.
[54] P. Giannozzi, S. Baroni, N. Bonini, M. Calandra, R. Car, C. Cavazzoni, D. Ceresoli, G.L. Chiarotti, M. Cococcioni, I. Dabo, A. Dal Corso, S. Fabris, G. Gougoussis, A. Kokalj, M. Lazzeri, L. Martin-Samos, N. Marzari, F. Mauri, R. Mazzarello, S. Paolini, A. Pasquarello, L. Paulatto, C. Sbraccia, S. Scandolo, G. Sclauzero, A.P. Seitsonen, A. Smogunov, P. Umari, R.M. Wentzcovitch, QUANTUM ESPRESSO: a modular and open-source software project for quantum simulations of materials, J. Phys. Condens. Matter 21 (2009) 395502.
[55] J.P. Perdew, A. Zunger, Self-interaction correction to density-functional approximations for many-electron system, Phys. Rev. B 23 (1981) 5048.
[56] J.P. Perdew, K. Burke, M. Ernzerhof, Generalized gradient approximation made simple, Phys. Rev. Lett. 77 (1996) 3865.
[57] G. Roman-Perez, J.M. Soler, Efficient Implementation of a van der Waals density functional: application to double-wall carbon nanotubes, Phys. Rev. Lett. 103 (2009) 096102.
[58] M. Dion, H. Rydberg, E. Schroder, D.C. Langreth, B.I. Lundqvist, Van der Waals density functional for general geometries, Phys. Rev. Lett. 92 (2004) 246401.
[59] K. Lee, E.D. Murray, L. Kong, B.I. Lundqvist, D.C. Langreth, Higher-accuracy van der Waals density functional, Phys. Rev. B 82 (2010), 081101(R).
[60] E.D. Murray, K. Lee, D.C. Langreth, Investigation of exchange Energy density functional accuracy for interacting molecules, J. Chem. Theory Comput. 5 (2009) 2754.
[61] J.P. Perdew, Y. Wang, Accurate and simple density functional for the electronic exchange energy: generalized gradient approximation, Phys. Rev. B 33 (1986) 8800.
[62] V.R. Cooper, Van der Waals density functional: an appropriate exchange functional, Phys. Rev. B 81 (2010) 161104.
[63] S. Grimme, Semiempirical GGA-type density functional constructed with a long-range dispersion correction, J. Comput. Chem. 27 (2006) 1787.
[64] S. Grimme, J. Antony, S. Ehrlich, H. Krieg, A consistent and accurate ab initio parametrization of density functional dispersion correction (DFT-D) for the 94 elements H-Pu, J. Chem. Phys. 132 (2010) 154104.
[65] G. Kresse, J. Hafner, *Ab initio* molecular dynamics for liquid metals, Phys. Rev. B 47 (1993) 558.
[66] G. Kresse, J. Hafner, *Ab initio* molecular-dynamics simulation of the liquid-metal-amorphous-semiconductor transition in germanium, Phys. Rev. B 49 (1994) 14251.
[67] G. Kresse, J. Furthmuller, Efficient iterative schemes for *ab initio* total-energy calculations using a plane-wave basis set, Phys. Rev. B 54 (1996) 11169.
[68] G. Kresse, J. Furthmuller, Efficiency of ab-initio total energy calculations for metals and semiconductors using a plane-wave basis set, Comput. Mater. Sci. 6 (1996) 15.
[69] A. Bostwick, T. Ohta, T. Seyller, K. Horn, E. Rotenberg, Quasiparticle dynamics in graphene, Nat. Phys. 3 (2007) 36.
[70] T.B. Ngwenya, A.M. Ukpong, N. Chetty, Defect states of complexes involving a vacancy in the boron site in boronitrene, Phys. Rev. B 84 (2011) 245425.
[71] C. Attaccalite, M. Bockstedte, A. Marini, A. Rubio, L. Wirtz, Coupling of excitons and defect states in boron-nitride nanostructures, Phys. Rev. B 83 (2011) 144115.
[72] G. Onida, L. Reining, A. Rubio, Electronic excitations: density-functional versus many-body Green's functions approaches, Rev. Mod. Phys. 74 (2002) 601.
[73] S.Y. Zhou, G.-H. Gweon, A.V. Fedorov, P.N. First, W.A. de Heer, D.-H. Lee, F. Guinea, A.H. Castro Neto, A. Lanzara, Substrate-induced bandgap opening in epitaxial graphene, Nat. Mater. 6 (2007) 770.
[74] P.E. Blochl, Projector augmented-wave method, Phys. Rev. B 50 (1994) 17953.
[75] H.J. Monkhorst, J.D. Pack, On Special points for brillouin zone integrations, Phys. Rev. B 13 (1976) 5188.
[76] M. Methfessel, A.T. Paxton, High-precision sampling for Brillouin-zone integration in metals, Phys. Rev. B 40 (1989) 3616.
[77] Y. Baskin, L. Mayer, Phys. Rev. 100 (1955) 544.
[78] W. Paszkowicz, J.B. Pelka, M. Knapp, T. Szyszko, S. Podsiadlo, Appl. Phys. A Mater. Sci. Process. 75 (2002) 431.
[79] G.C. Capitani, S. Di Pierro, G. Tempesta, Am. Mineral. 92 (2007) 403.
[80] M.W. Finnis, The theory of metal-ceramic interfaces, J. Phys. Condens. Matter 8 (1996) 5811.
[81] T. Hong, J.R. Smith, D.J. Srolovitz, Theory of metal-ceramic adhesion, Acta Metall. Mater. 43 (1995) 2721.
[82] E. Lampin, C. Priester, C. Krzeminski, L. Magaud, J. Appl. Phys. 107 (2010) 103514.
[83] G. Sclauzero, A. Pasquarello, Microelectron. Eng. 88 (2011) 1478.
[84] R.V. Gorbachev, A.K. Geim, M.I. Katsnelson, K.S. Novoselov, T. Tudorovskiy, I.V. Grigorieva, A.H. MacDonald, S.V. Morozov, K. Watanabe, T. Taniguchi, L.A. Ponomarenko, Coulomb drag and broken symmetry in double-layer graphene, Nat. Phys. 8 (2012) 896.
[85] B. Sachs, T.O. Wehling, M.I. Katsnelson, A.I. Lichtenstein, Adhesion and electronic structure of graphene on hexagonal boron nitride substrates, Phys. Rev. B 84 (2011) 195414.
[86] F. Sols, F. Guinea, A.H. Castro Neto, Coulomb blockade in graphene nanoribbons, Phys. Rev. Lett. 99 (2007) 166803.
[87] M.Y. Han, J.C. Brant, P. Kim, Electron transport in disordered graphene nanoribbons, Phys. Rev. Lett. 104 (2010) 056801.
[88] G.M. Rutter, S. Jung, N.N. Klimov, D.B. Newell, N.B. Zhitenev, J.A. Stroscio, Microscopic polarization in bilayer graphene, Nat. Phys. 7 (2011) 649.
[89] A.C. Ferrari, J.C. Meyer, V. Scardaci, C. Casiraghi, M. Lazzeri, F. Mauri, S. Piscanec, D. Jiang, K.S. Novoselov, S. Roth, A.K. Geim, Raman spectrum of graphene and graphene layers, Phys. Rev. Lett. 97 (2006) 187401.
[90] Z. Ni, Y. Wang, T. Yu, Z. Shen, Raman spectroscopy and imaging of graphene, Nano Res. 1 (2008) 273.